Received: 22 August 2018 | Revised: 9 October 2018 | Accepted: 26 October 2018

DOI: 10.1002/jmr.2771

RESEARCH ARTICLE

WILEY Journal of Molecular Recognition

Exploring aggregation-induced emission through tuning of ligand structure for picomolar detection of pyrene

Milan Ghosh[1] | Sabyasachi Ta[1] | Sisir Lohar[2] | Sudipta Das[3] | Paula Brando[4] | Vitor Felix[4] | Debasis Das[1]

[1] Department of Chemistry, The University of Burdwan, Bardhaman, India

[2] Department of Chemistry, T. D. B. College, Raniganj, Bardhaman, India

[3] Department of Chemistry, Raina Swami Bholananda Vidyayatan, Bardhaman, India

[4] Department of Chemistry, CICECO–Aveiro Institute of Materials, University of Aveiro, Aveiro, Portugal

Correspondence
Debasis Das, Department of Chemistry, The University of Burdwan, Bardhaman 713104, India.
Email: ddas100in@yahoo.com

Abstract

Tuning of ligand structures through controlled variation of ring number in fused-ring aromatic moiety appended to antipyrine allows detection of 7.8×10^{-12} M pyrene via aggregation-induced emission (AIE) associated with 101-fold fluorescence enhancement. In one case, antipyrine unit is replaced by pyridine to derive bis-methylanthracenyl picolyl amine. The structures of four molecules have been confirmed by single crystal X-ray diffraction analysis. Among them, pyrene-antipyrine conjugate (L) undergoes pyrene triggered inhibition of photo-induced electron transfer (PET) leading to water-assisted AIE.

KEYWORDS

AIE, pyrene, SC-XRD, sensor, SPE

1 | INTRODUCTION

The design and development of appropriate fluorescence probe for selective detection and monitoring of toxic molecules have been a subject of interest in the modern research area.[1] Polycyclic aromatic hydrocarbons (PAHs) are widely distributed and relocated in the environment as a result of incomplete combustion of organic matter.[2] Reactive PAHs belong to 10 most toxic classes of organic compounds (by Centre for Disease Control in 2011)[3-7] for cell damaging, cytotoxicity, mutagenicity, damage of nervous system, chemical modification of protein, and nucleic acid. Pyrene imparts toxicity in living organisms from bacteria to plants and animals. Its epoxides are highly toxic, mutagenic and/or carcinogenic to microorganisms and higher systems including humans.[8] Several pyrene derivatives causes skin, lung, bladder, liver, and stomach cancers. Being hydrophobic, it easily permeates cell membrane and accumulates in lipid tissues.[9-12] The benzopyrene, a metabolites of pyrene binds to DNA to cause lung cancer.[13] Moreover, relatively high water solubility of pyrene over higher PAHs allows to spread in living systems through grains, fruits, vegetables, drinking water, and meat[14]. Inhalation of combustion products and coal tar linings[15] and dry cleaning of garments are also responsible for pyrene poisoning.[16,17] The above discussion clearly indicates the immense importance of trace level selective detection and estimation pyrene, which is difficult because of similar properties PAHs.[18,19] It is to be noted that most of the PAHs, including pyrene, are prone to aggregation (monomer to excimer) in solution, the main obstacle for their selective recognition. The literature suggests that the present optical probe is the first of its kind that selectively recognizes pyrene through PET-AIE mechanism.[20-25] Additionally, high-florescence lifetime and quantum yield of pyrene excimer may be useful for solar energy storage system.[26]

The present probe, a pyrene–antipyrine conjugate (L) undergoes pyrene-induced AIE through π-π stacking. L is characterized by ^{1}HNMR, UV–Vis, steady state and time-resolved fluorescence, fourier-transform infrared spectroscopy (FTIR), ESI-MS spectroscopy, and single-crystal XRD analysis (Figure S1-S20, ESI). Density functional theory (DFT) studies support the experimental facts. The developed method is applied for the determination pyrene[2] in water from Gomti river (India). Solid phase extractive separation of pyrene has been achieved.

2 | RESULT AND DISCUSSION

Five probes, viz, L, L1, L2, L3, and L4 have been synthesized (Scheme 1). L displays very weak emission at 475 nm upon excitation

CCDC No: 1562252 (L), 1562217(L1), 1562244 (L3), 1562253 (L4)

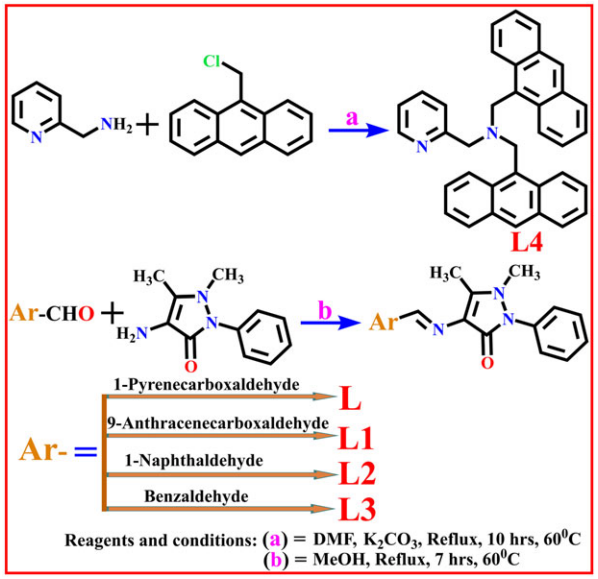

SCHEME 1 Synthesis of probes

at 384 nm (Figure S4, ESI). Similarly, L1, L2, L3, and L4 exhibit weak emissions at 396, 376 and 522, 444, and 396 nm upon excitation at 340, 342, 396, and 318 nm, respectively.

Pyrene perturbs steady state emission (λ_{Em}, 498 nm) of L at picomolar level while other tested common PAHs (λ_{Ex}, 384 nm) viz naphthalene (λ_{Em}, 332 nm), anthracene (λ_{Em}, 411 nm), anthanthrene (λ_{Em}, 418 nm), acenaphthene (λ_{Em}, 330 nm), acephenanthrene (λ_{Em}, 297 nm), acridine (λ_{Em}, 443 nm), phenanthrene (λ_{Em}, 289 nm), chrysene (λ_{Em}, 303 nm), benzo [a] pyrene (λ_{Em}, 414 nm), benzo [g] chrysene (λ_{Em}, 397 nm), perylene (λ_{Em}, 285 nm), and picene (λ_{Em}, 289 nm) remain silent (Figure 1). The pyrene-assisted green emission of L is very distinct and highly selective. Several model probes have been synthesized to unveil the underlying sensing mechanism of pyrene. Subtle tuning of the structure of ligand (L) by varying the appended unit to antipyrine results, L1 (appended unit is anthracene, λ_{Ex} = 340 nm, λ_{Em} = 482 nm) and L2 (appended unit is naphthalene, λ_{Ex} = 342 nm, λ_{Em} = 477 nm). However, neither L1 nor L2 undergo pyrene assisted significant fluorescence enhancement like L (Figure S21–22, ESI). Moreover, L detects pyrene without any interference from other common PAHs (Figure S23, ESI). On the other hand, L3 and L4 are unable to detect pyrene. Figures S24 and 25 (ESI) show interference suffered during pyrene detection by L1 and L2.

The emission profiles of L, L1, and L2 (Figure S26, ESI) indicate no significant change at pH range, 3.0 to 12.0, suggesting their usefulness at physiological pH. Therefore, entire studies have been performed at pH 7.4 using HEPES buffered aqueous DMSO (20mM, DMSO/H_2O; 4/1, v/v). However, other media like aqueous MeOH (MeOH/H_2O; 4/1, v/v), aqueous CH_3CN (CH_3CN/H_2O; 4/1, v/v) and aqueous DMF (DMF/H_2O; 4/1, v/v) have also been tested. Changes in emission intensity being maximum in aqueous DMSO (DMSO/H_2O; 4/1, v/v) are used for the entire studies.

Figure 2A represents the changes of emission spectra of L upon gradual addition of pyrene (DMSO/H_2O, 4/1, v/v, pH 7.4). Upon gradual addition of pyrene to L, the emission intensity of the pyrene monomer at 393 nm decreases while that of excimer increases at 498 nm with an isoemissive point at 460 nm (Figure S27, ESI). This is due to the π-π stacking of pyrene unit of L with pyrene analyte. This red shift of the emission is accompanied by 101- and 36.7-fold enhancement of

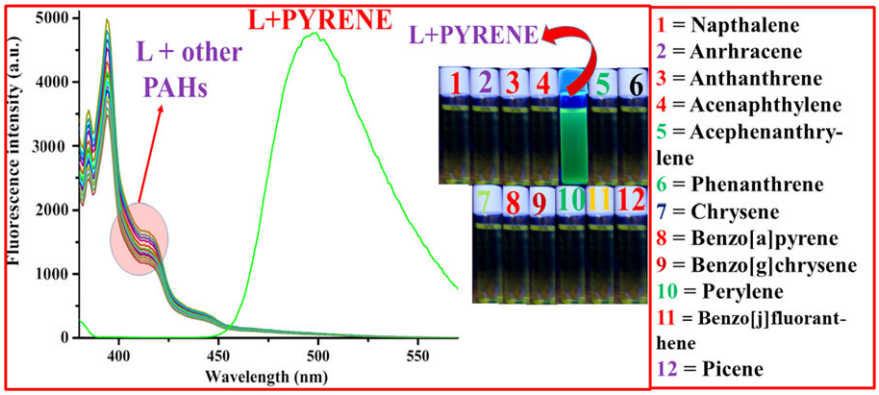

FIGURE 1 Emission spectra of L (20 μM, DMSO/H_2O, 4/1, v/v, 20mM HEPES buffer, pH 7.4) in presence of common PAHs (λ_{Ex}, 384 nm)

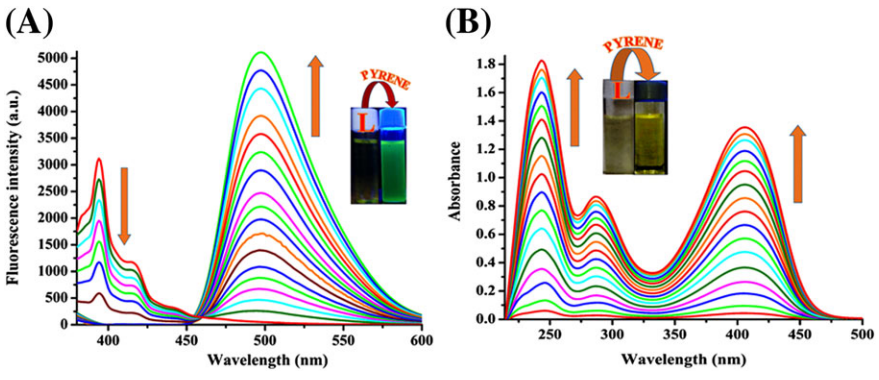

FIGURE 2 Changes in (A) emission and (B) absorption spectra of L (20 μM) in HEPES-buffered (20mM, DMSO/H_2O, 4/1, v/v, pH 7.4) solution upon gradual addition of pyrene (0.0, 0.005, 0.01, 0.05, 0.1, 0.5, 1.0, 2.0, 5.0, 10, 20, 30, 50, 75, 100, 200, 300, 500, 1000, 1500, 2000, 2500, and 3000 μM) (λ_{Ex}, 384 nm)

fluorescence intensity and quantum yield, respectively (λ_{Ex}, 384 nm; Φ, 70.27). In presence of pyrene, L1 (λ_{Ex}, 340 nm) and L2 emit at 482 and 477 nm (λ_{Ex}, 342 nm, Figure S28, ESI), respectively. Upon gradual addition of pyrene to L1 or L2, the emission intensity at 388 (L1) and 393 nm (L2) decreases gradually with concominant increase at 482 (L1) and 477 nm (L2) associated with isoemissive points at 408 (L1) and 449 nm (L2), respectively (Figure S29–30, ESI). This pyrene-assisted fluorescence enhancement is attributed to the π-π stacking of anthracene and naphthalene moieties (L1 and L2) with pyrene. Figure 2A and S28 (ESI) clearly indicate that the decrease in the number of rings of PAH blue shifts the emission band from 498 (L) to 482 (L1) to 475 nm (L2), and at the same time, the emission intensity decreases significantly. Probably benzene moiety of L3 fails π-π stacking with pyrene as no fluorescence enhancement is observed (Figure S31, ESI). Despite having two anthracene units, L4 also fails to π-π stacking and hence, to recognize pyrene. This is because two anthracene rings lie in different planes that also differ from the pyridine unit, revealed from its single crystal X-ray structure (Figure S32, ESI and Scheme 2).

The plots of emission intensity versus pyrene concentration for L, L1, and L2 are presented in Figure S33–35 (ESI). The LODs[2g, h] of L, L1, and L2 for pyrene are 2×10^{-12} M, 2×10^{-9} M, and 5×10^{-9} M while respective association constants are 3.81×10^{6} M^{-1}, 7.60×10^{5} M^{-1}, and 2.09×10^{5} M^{-1}, determined applying the Hill equation[27] (Figure S36–38, ESI). Moreover, the LOD of L for pyrene is 7.8×10^{-12} M following 3σ/K method[2d–f] where σ is the standard deviation of the blank, and K is the slope of the calibration curve (Figure S33, ESI, inset plot). Thus, L is effective for detection of pyrene in river and tap water samples.[2] The Job's plot[28] indicate 1:1 (mole ratio) interaction between probe and pyrene (Figure S39–41, ESI).

In the presence of pyrene, the very weak absorption of L is blue shifted from 406 to 403 nm and increases gradually with increasing pyrene concentration (Figure 2B). Besides, two new absorption bands that appear at 246 and 293 nm also increase gradually. On the other hand, two new absorption bands that appear at 373 and 325 nm upon addition of pyrene to L1 and L2 also increase gradually with increasing pyrene concentration. In the presence of pyrene, the gradual blue shift of absorption band from 403 (L) to 373 (L1) to 325 nm (L2) is probably due to lesser π-π stacking between the probe and pyrene (Figure S42, ESI). This notion is obvious because with increasing conjugation of the probe with increasing number of appended aromatic nucleus enhances π-π stacking between the probe and pyrene. Thus, for L3, it is less (Figure S43, ESI) while little better for L4 (Figure S44, ESI) as reflected from the absorption spectrum. However, the π-π stacking is relatively poor for L4 as appended anthracence units being attached to the sp^3 N are out of plane and hence extended conjugation is not feasible. Consequently, π-π stacking of L4 with pyrene is much less than it could be for a planar molecule.

It is already mentioned that very weak emission of L is attributed to the PET process from imine N to the photo-excited pyrene moiety. The fluorescence of L at 498 nm enhances in the presence of pyrene in DMSO medium due to π-π stacking of pyrene units of L with externally added pyrene leading to formation of dynamic excimer where syn- and anti- forms of L remain in equilibrium. Interestingly, upon addition of water to the system, hydrogen bonds involving imine N and water O stabilize the syn- forms of L, and consequently, external pyrene accommodates in between two pyrene units of two L leading to formation of stable static excimer. Hence, significant fluorescence enhancement occurs through water-assisted aggregation involving L and external pyrene (Scheme 3), termed as AIE. The presence of an isoemissive point at 460 nm indicates the existence of two different species at equilibrium (Figure S27, ESI). In the absence of external pyrene, steric crowding of methyl group attached to antipyrine of L restricts two pyrene units from two L to come sufficiently closer and parallel for π-π stacking (homo) to occur. In the absence of external pyrene, addition of water even fails to enhance the fluorescence (Scheme 3). However, upon addition of external pyrene, it accomodates in between two probes (L) and qualify the distance required to form π-π stacking (hetero) with the pyrene units of L and escapes the steric hindrance mentioned supra. Thus, pyrene assisted dynamic excimer equilibrium between syn- and anti- forms of L turns into static excimer where the syn- conformation is stabilized through water-assisted intermolecular hydrogen bonding. This kind of observations are absent for L1 and L2. Although, the anthracene unit of L1 is capable of π-π stacking with external pyrene, probably it is not strong enough to form stable static excimer leading to AIE in the presence of water. Similarly, L2 containing naphthalene moiety has further less π-π stacking efficiency in the series with external pyrene fails to show water-assisted AIE.

FTIR spectra[29] of L, L1, and L2 and their pyrene adduct support their interactions (Figure S45-S47, ESI).

The dynamic light scattering (DLS) studies also support aggregation of L in the presence of pyrene. At constant concentration of L (20 μM) in a particular solvent, increasing pyrene concentration increases the average particle size (Z_{av}) in solution. The value of Z_{av} increases from 165 to 240 nm upon increase of pyrene concentration from 1000 to 1300 μM in DMSO/H_2O (4/1, *v*/v, pH 7.4), indicating pyrene triggered aggregation of L (20 μM). Moreover, Z_{av} further

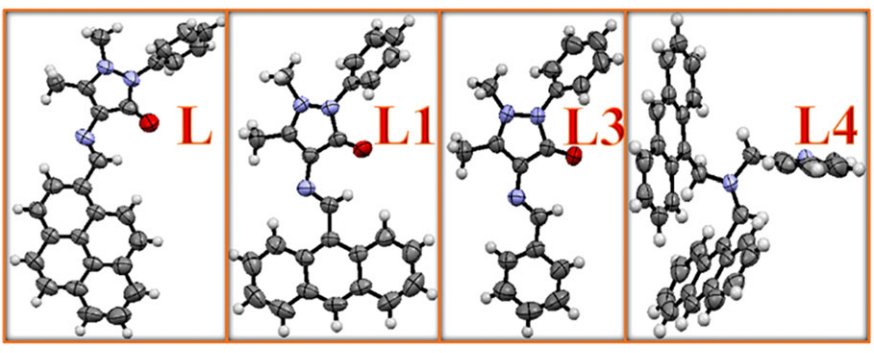

SCHEME 2 SCXRD structures of probes

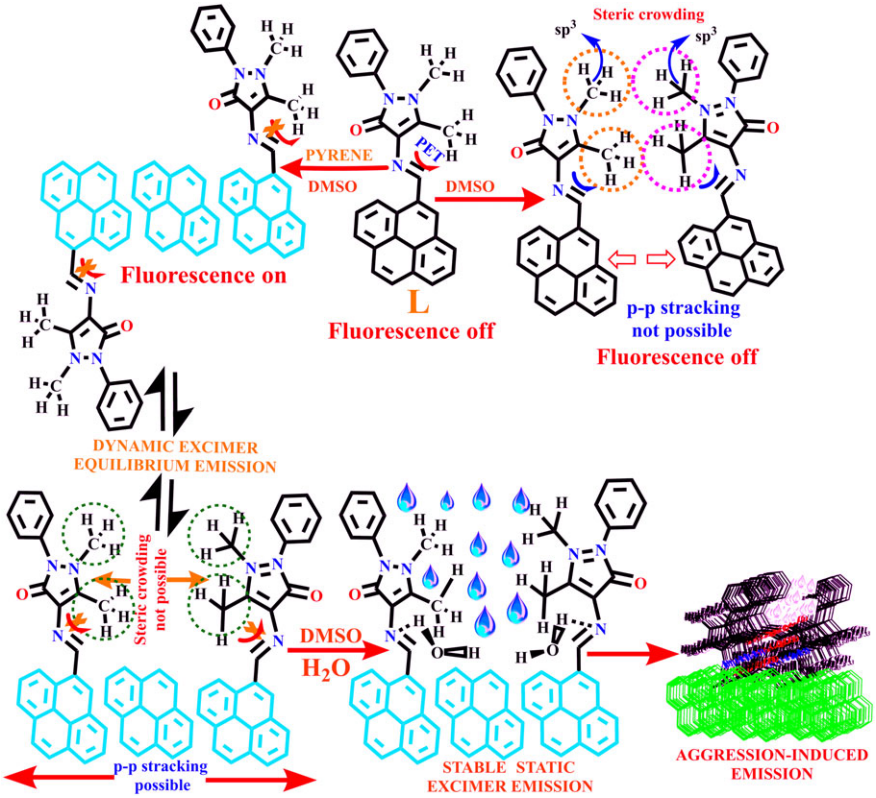

SCHEME 3 Sensing mechanism

increases from 735 to 828 nm with increasing water percentage, keeping concentration of L and pyrene unaltered. This highlights the role of water towards AIE (Figure S48, ESI). For L1 and L2, no aggregation is observed.

The ^{1}HNMR titration is performed by gradual addition of pyrene to L (Figure 3). Addition of 0.5 equiv pyrene to L up field shifted alkyl protons from 3.388 to 3.253 ppm, indicating some sort of interaction. Addition of 1 equiv pyrene, further shifted those protons up field to 3.179 ppm, indicating stronger interaction. Moreover, addition of 0.5 equiv pyrene to L shifted "a" proton (labeled in Figure S2, ESI) up field from 9.812 to 9.631 ppm, probably due to hydrogen bonding between N center of antipyrene moiety (L) with water present in DMSO-d_6. The aromatic "b" proton also shifted up field. Additionally, all aromatic protons up field shifted from 7.892 to 7.505 ppm because of increased electron density in the ring via π-π interaction with added pyrene that accommodates itself in between two pyrene units of two L, forming excimer, a step forward towards aggregation at higher-pyrene concentration. At higher-pyrene concentration, in addition to up field shift of the protons, peak broadening occurs, probably because of exchange of L molecules between free and aggregated state (Figure 3).

Effect of added water on the emission characteristics of [L-pyrene] system in DMSO have been investigated (Figure S49a, ESI). The emission intensity of L (λ_{Em}, 498 nm) enhances approximately 41-fold at 60% water (v/v) and 52-fold at 90% water (v/v). Further increase of water content intensifies the emission intensity further; however, turbidity appears, a signature of aggregation ascribed to AIE process.[30] The AIE process is also reflected in absorption spectroscopic studies. Gradual increase of water (25-75%, v/v) to the DMSO solution of [L-pyrene] system broadens and red shifts the absorption peak from 406 to 436 nm (Figure S49b, ESI). On the other hand, this kind of water-assisted pyrene-induced aggregation are absent in L1 and L2. These facts are demonstrated in a snapshot in Figure S50 (ESI) where emission peaks associated with free L, pyrene monomer (393 nm), excimer (475 nm), and pyrene-induced water-assisted AIE of L (498 nm) are captured altogether. It is to be noted that the ratio of emission intensity (EI), viz, EI $_{[L\text{-pyrene}]}$ at 498 nm/EI $_{[pyrene]}$ at 475 nm is 15.3 (DMSO/H_2O, 2/3, v/v, pH 7.4).

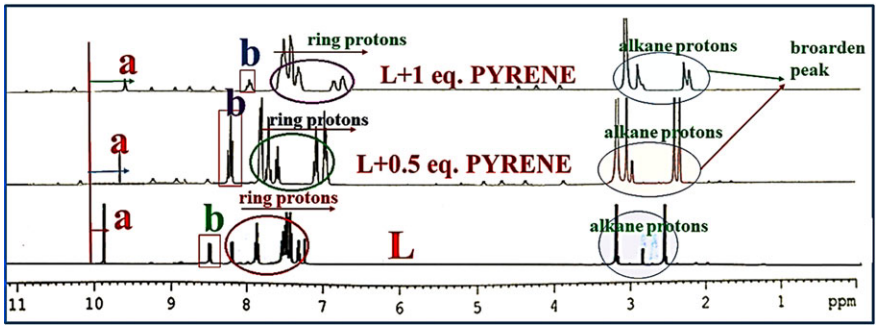

FIGURE 3 ^{1}HNMR spectra of L in absence and presence of pyrene in DMSO-d_6: (1) L; (2) L + 0.5 equiv pyrene; (3) L + 1.0 equiv pyrene

The fluorescence lifetime data corroborates the proposed sensing mechanism (Figure S51–53, ESI). The average lifetime of L is 0.759 ns in DMSO. In the presence of pyrene (L: pyrene = 2: 1, mole ratio), the fluorescence lifetime significantly increases to 5.7258 ns in DMSO. Increasing water enhances the fluorescence lifetime gradually from 51.4773 ns (25%, v/v) to 106.1560 ns (30%, v/v) to 206.1660 ns (50%, v/v), respectively. At the same time, quantum yield[31] (ϕ) also increases from 3.13% to 27.83% to 37.13%.

3 | APPLICATION

3.1 | Real sample analysis and solid phase extractive removal of pyrene

The developed method has been applied[2a–c] for pyrene determination in river and tap water samples following standard addition method (Table S6, ESI). To evaluate the accuracy of the method, recovery studies have been performed at different concentration levels. A known amount of pyrene (Table S6, ESI) is added to water sample collected from Gomati river (a tributary of the river Ganga, one of the most polluted rivers in India). Total concentration of pyrene is determined using the developed method. The L, immobilized on silica, is highly efficient for SPE removal of pyrene from real samples (Figure S54 and Table S7, ESI).

4 | CONCLUSION

A simple antipyrine–pyrene conjugate (L) has been exploited for detection of picomolar (7.8×10^{-12} M) pyrene in aqueous-DMSO media through generation of green fluorescence via water-assisted AIE mechanism. The extent of association between L and pyrene is determined by the Hill equation ($K_a = 3.81 \times 10^6$ M^{-1}). The developed method determines concentration of pyrene in Gomti river water.

5 | EXPERIMENTAL

5.1 | Materials and equipment

High-purity buffer HEPES, 1-pyrenecarboxaldehyde, 9-anthracene carboxaldehyde, 1-naphthaldehyde, benzaldehyde, 2-picolylamine, 9-chloromethyl anthracene, and 4-aminoantipyrene have been purchased from Sigma–Aldrich (India). The solvents used has spectroscopic grade. Other molecules and salts are also purchased from Merck (India). Other analytical reagent grade chemicals are used without further purification unless specified otherwise. Milli-Q Millipore 18.2 MΩ cm^{-1} water is used whenever required. A Shimadzu Multi Spec 2450 spectrophotometer is used for recording UV–vis spectra. FTIR spectra are recorded on a Shimadzu FTIR (model IR Prestige 21 CE) spectrophotometer. Mass spectra are recorded using a QTOF 60 Micro YA 263 mass spectrometer in ES positive mode. The steady state emission and excitation spectra have been recorded with a Hitachi F-4500 spectrofluorimeter. Time-resolved fluorescence lifetime measurements are performed with a picosecond pulsed diode laser-based time-correlated single-photon counting (TCSPC) spectrometer (IBH, UK, λ_{ex} = 384 nm) coupled to MCP-PMT detector (model FL-1057). A Systronics digital pH meter (model 335) is used for pH measurement. ^{1}HNMR spectra are recorded on a Bruker Avance III HD (400 MHz) spectrometer. Chemical shifts are reported in parts per million (ppm), and the residual solvent peak is used as an internal reference: tetramethylsilane (TMS, δ 0.00) is used as a reference. Multiplicity are indicated as follows: s (singlet), d (doublet), t (triplet), q (quartet), m (multiplet). Coupling constants are reported in Hertz (Hz).

5.2 | Synthesis of L

The probe, L is synthesized by refluxing of equimolar mixture of 1-pyrenecarboxaldehyde (0.50 g, 2.1 mol) and 4-aminoantipyrine (0.43 g, 2.1 mol) in methanol for 7 h at 60°C (Scheme 1). The brown-yellow crystals are found after few days by slow evaporation of the solvent. Yield is 95%. Anal. calcd. (%): C, 80.55; H, 5.55 and N, 10.06; found: C, 80.83; H, 5.86 and N, 9.95. Single crystal of L, suitable for X-ray diffraction is mounted on a Bruker SMART APEX CCD diffractometer at 296 K and diffracted by Mo-K_α radiation (λ = 0.71073 Å). The crystal belongs to P21/n space group. The crystal parameters and refinement details are listed in Table S1 (ESI). The bond angles and lengths are detailed in Table S2 (ESI). The QTOF–MS ES^+ (Figure S1, ESI): m/z for $[M + H]^+$ found at 419.60 (-100%), (calcd. 419.18) and $[M + Na]^+$ at 441.76 (-40%). The ^{1}HNMR spectra is recorded in DMSO-d_6 at 25°C; δ (ppm) (Figure S2, ESI): 10.616 (1H, s), 8.907–8.886 (1 H, s), 8.243–7.887 (4H, d, J = 6.8), 7.592–7.282 (m, J = 1.6), δ; 3.203–2.572. The experimental FTIR (cm^{-1}) spectra is shown in Figure S3 (ESI): υ (O-H), 3714; υ(-C-H-), 2988 and 2874; υ(-C=N-), 1616; υ(-C=C-), 1578 and 1559; υ(C-H), 1477; υ(-C-O-), 1313; υ(-C-N-), 1080. The UV–vis. Spectrum of L (DMSO/H_2O, 4/1, *v*/v, 20mM HEPES, pH 7.4) have three bands, *viz*. 240 nm, 288 nm, and 406 nm (Figure S4, ESI). The intense 240 nm band ($\varepsilon = 9.85 \times 10^3$ M^{-1} cm^{-1}) is assigned to π-π* transition while the weak band at 288 nm ($\varepsilon = 1.22 \times 10^2$ M^{-1} cm^{-1}) is due to π-π* transition at lower energy. The strong band at 306 nm ($\varepsilon = 5.22 \times 10^3$ M^{-1} cm^{-1}) is attributed to n-π* electron transition from non-bonding terminal N of imine moiety to an anti-bonding orbital of L. The excitation of L at 384 nm resulted emission at 475 nm (DMSO/H_2O, 4/1, v/v, 20mM HEPES, pH 7.4, Figure S4, ESI).

5.3 | Synthesis of L1

Anthracene-9-carbaldehyde (1 g, 6.09 mmol), dissolved in methanol is added to methanol solution of 4-aminoantipyrine (1.23 g, 6.09 mmol) (Scheme 1). The mixture is refluxed for 7 hours at 60°C. Slow evaporation of solvent resulted L1 in 95% yield. The brown–yellow crystals are observed after slow evaporation of the solvent. Yield is 95%. Anal calcd (%): C, 79.13; H, 5.58 and N, 11.07; found: C, 79.52; H, 5.50 and N, 9.97. Single crystal of L1, suitable for X-ray diffraction is diffracted as narrated for L. The crystal belongs to P21 space group. The crystal parameters and refinement data are listed in Table S1 (ESI). The

selected bond angles and lengths are detailed in Table S3 (ESI). The QTOF–MS ES$^+$ (Figure S5, ESI) shows m/z for [M + Na]$^+$ (approximately 100%) at 414.14 and 392.15 for [M + H]$^+$ (approximately 35%) (calcd. 392.17) while m/z at 424.15 for [M + CH_3OH + H]$^+$ (approximately 15%) (calcd 424.51). A low abundance peak is observed at m/z 224.48, probably due to water adduct of the fragmented anthracene aldehyde. The ^{1}HNMR (Figure S6, ESI) ($CDCl_3$), δ (ppm): 8.238 (1H, s) for (–N=C-H) assigned as "j" proton; 7.679 (1H, m) for "e" proton; 7.259–6.831 (11H, m, J = 9.2); 2.835–2.742 are aliphatic protons. The experimental FTIR (cm^{-1}) spectra is shown in Figure S7 (ESI); 2958 and 2899, υ(-C-H-); 1616, υ(-C=N-); 1407, υ(-C=C-); 1313, υ(-C-O-); 1049, υ(-C-H-); 3342, υ(-O-H-). The absorption spectrum of L1 (Figure S8, ESI) (DMSO/H_2O, 4/1, *v*/v, 20mM HEPES, pH 7.4) shows two bands at 256 nm and 365 nm. The intense band at 256 nm (ε = 8.48 × 10^2 M^{-1} cm^{-1}) is assigned to π-π* electron transition while the weak band at 365 nm (ε = 1.22 × 10^2 M^{-1} cm^{-1}) is due to n- π* electron transition of non-bonding electron on terminal N of imine moiety to anti-bonding orbital of L1. The excitation of L1 at 340 nm results emission at 396 nm (DMSO/H_2O, 4/1, v/v, 20mM HEPES, pH 7.4, Figure S8, ESI).

5.4 | Synthesis of L2

Naphthalene-1-carboxaldehyde (1 g, 6.40 mmol) is dissolved in 10 mL methanol and added to 10 mL methanol solution of 4-aminoantipyrine (1.29 g, 6.40 mmol) (Scheme 1. The mixture is refluxed for 7 h at 60°C. Slow evaporation of solvent resulted solid L2 with 95% yield. Anal. calcd (%): C, 77.40; H, 5.61 and N, 12.31; found: C, 77.62; H, 5.50 and N, 12.25. The MS ES+ (Figure S9, ESI): m/z for [M + H]$^+$ = 342.25 (calcd. 342.41) (- 22%); 364.30 (calcd. 364.14) for [M + Na]$^+$ (100%) and 396.34 (calcd. 396.52) for [M + CH_3OH + Na]$^+$. The peak having 35% abundance at 157.09 (calcd. 157.18) indicates the molecular ion peak of naphthalene-1-carboxaldehyde. The ^{1}HNMR (Figure S10, ESI) ($CDCl_3$), δ (ppm): 10.594 (1H, s) refers to (–N=C-H) denoted as "h"; 8.888 (1H, d, J = 8.4) for "g" proton; 8.219 (1H, t, J = 6.8) for "a" proton; 7.904–7.864 (2H, q, J = 7.6) for "d" and "e" protons; 7.572–7.259 (m, J = 2) for aromatic protons; 3.181 and 2.551 for aliphatic protons. The FTIR (cm^{-1}) spectrum (Figure S11, ESI): 2972, υ(-C-H-); 1645, υ(-C=N-); 1565 and 1477, (-C=C-); 1298 υ(-C-O-); 1066, υ(-C-H-). The absorption spectrum of L2 (Figure S12, ESI) (DMSO/H_2O, 4/1, *v*/v, 20mM HEPES, pH 7.4) shows the intense band at 282 nm (ε; 3.44 × 10^3 M^{-1} cm^{-1}), assigned to π-π* electron transition. Another band at 417 nm (ε = 1.65 × 10^2 M^{-1} cm^{-1}) is due to n- π* electron transition from non-bonding electron on terminal N of imine moiety to the anti-bonding orbital of L2. The excitation of L2 at 342 nm leads the emission at 376 and 522 nm (DMSO/H_2O, 4/1, v/v, 20mM HEPES, pH 7.4, Figure S12, ESI).

5.5 | Synthesis of L3

Benzaldehyde (1 g, 9.42 mmol), dissolved in methanol, is added to methanol solution of 4-amino-antipyrine (1.91 g, 9.42 mmol) (Scheme 1). The mixture is refluxed for 7 hours at 60°C. Slow evaporation of the solvent resulted L3 in 95% yield. The yellow crystals are observed after slow evaporation of the solvent. Anal calcd (%): C, 74.20; H, 5.88 and N, 14.42; found: C, 74.36; H, 5.80, and N, 14.33. Single crystal of L3, suitable for X-ray diffraction, is analyzed at 296 K as mentioned supra. The crystal belongs to P 21/c space group. The crystal parameter and refinement details are listed in Table S1 (ESI). The bond angles and lengths are detailed in Table S4 (ESI). The QTOF–MS ES+ (Figure S13, ESI): m/z for [M + H]$^+$ = 292.33 (calcd 292.35) (-100%); [M + Na]$^+$ = 314.34 (calcd 314.35) (10%). The ^{1}HNMR (Figure S14, ESI) ($CDCl_3$), δ (ppm): 9.763 (1H, s) refers to imine proton (-N=C-H) denoted as "f"; 7.871 (1H, s) for "a" proton; 7.866 (1H, d, J = 1.6) for "e" proton; 7.499–7.259 (8H, m, J = 9.2) for aromatic protons; 3.153 and 2.494 for aliphatic protons. The FTIR (cm^{-1}) spectrum is shown in Figure S15 (ESI): 2912 and 2975, υ(-C-H-); 1630 υ(-C=N-); 1610 and 1565, υ(-C=C-); 1395, υ(-C-H-); 1047, υ(-C-O-), and 3367, υ(-O-H). The UV–vis spectrum of L3 (Figure S16, ESI, DMSO/H_2O, 4/1, *v*/v, 20mM HEPES, pH 7.4) shows absorbance at 252 nm (ε = 3.44 × 10^3 M^{-1} cm^{-1}), assigned to π-π* electron transition. The band at 342 nm (ε = 1.55 × 10^2 M^{-1} cm^{-1}) is due to n- π* electron transition from nonbonding terminal N of imine moiety to an antibonding orbital of L3. The excitation of L3 at 396 nm leads the emission at 444 nm (DMSO/H_2O, 4/1, v/v, 20mM HEPES, pH 7.4, Figure S16, ESI).

5.6 | Synthesis of L4

Dry DMF solution of 9-chloromethylanthracene (1 g, 8 mmol) is stirred with anhydrous K_2CO_3 for 1 hour followed by addition of 2-picoylamine (1.26 g, 8 mmol). The mixture is stirred for 15 hours followed by reflux for 10 hours at 60°C. The solvent is removed using rotary evaporator, and the residue is partitioned with ethylacetate and water. Upon removal of solvent, the target compound L4 (0.8 g 4.76 mmol) is isolated (Scheme 1) and recrystallized as dirty white crystal from methanol solution. Anal calcd (%): C, 83.26; H, 5.95; and N, 10.79; found: C, 83.52; H, 5.91 and N, 10.57. Single crystal of L4, suitable for X-ray diffraction, is analyzed similarly as described supra at 100 K. The crystal belongs to P-1 space group. The crystal parameter and refinement data are listed in Table S1 (ESI). The bond angles and lengths are detailed in Table S5 (ESI). The QTOF–MS ES$^+$ (Figure S17, ESI): m/z for [M + H]$^+$ = 489.48 (calcd. 489.58) (approximately 100%); [M + Na]$^+$ = 511.40 (calcd 511.42) (approximately 25%); the ^{1}HNMR spectrum (Figure S18, ESI) ($CDCl_3$), δ (ppm): 10.998 (1H, s) for (-N=C-H-) denoted as "j"; 8.943 (1H, s) for "a" and "i" proton; 8.920 (1H, d, J = 1.6); 8.243–8.007 (3H, m, J = 6.8) for aromatic protons; 7.563–7.282 (8H, m, J = 8.4) for aromatic protons; 3.240 for "n" and 2.853 and 2.636 for aliphatic protons (p, o). The FTIR (cm^{-1}) spectrum (Figure S19, ESI): 2962 and 2880, υ(-C-H-); 1673 υ(-C=N-); 1560 υ(-C=C-); 1445, υ(-C-H-); 1035, υ(-C-N-), 3348, υ(-O-H). The UV–vis spectrum of L4 (Figure S20, ESI, DMSO/H_2O, 4/1, *v*/v, 20mM HEPES, pH 7.4) has a peak at 257 nm (ε = 3.44 × 10^5 M^{-1} cm^{-1}), assigned to π-π* electron transition. The band at 376 nm (ε = 1.69 × 10^3 M^{-1} cm^{-1}) is due to n- π* electron transition from nonbonding electron on terminal imine N to an antibonding orbital of L4. The excitation of L4 at 318 nm leads the emission at 396 nm (DMSO/H_2O, 4/1, v/v, 20mM HEPES, pH 7.4).

ACKNOWLEDGEMENTS

M.G. sincerely acknowledges CSIR (New Delhi) for fellowship. S.T. and D.D. thank UGC-DAE-Kolkata and Department of Environment, Gov WB for financial assistance.

CONFLICT OF INTERESTS

No conflict of interest to report.

AUTHORS' CONTRIBUTIONS

M.G. synthesized all the compounds and characterized them. S.T. solved some single crystal X-ray structures. S.L. grew some single crystals of the compounds. S.D. performed some solution phase experiments. P.B. solved few single crystal X-ray structures. V.F. refined and wrote single crystal X-ray structures. The idea of this research is the brainchild of D.D., one of the corresponding authors.

ORCID

Debasis Das http://orcid.org/0000-0003-0474-0842

REFERENCES

1. Germain ME, Knapp MJ. Optical explosives detection: from color changes to fluorescence turn-on. *Chem Soc Rev*. 2009;38(9):2543-2555.
2. (a) Nandi S, Adhikari S, Mandal S, Banerjee A, Das D. Tuning FRET efficiency as a novel approach for improved detection of naphthalene: application to environmental samples. *J Mol Recog*. 2016;29(7):303-307. (b) Ghosh M, Ta S, Banerjee M, Mahiuddin M, Manna PP, Das D. A hydrogen bond assisted CHEF approach for colorimetric and fluorescence recognition of picric acid and its solid phase extraction by an immobilized probe. *ChemistrySlect*. 2018;3(22):6145-6151. (c) Ghosh M, Ta S, Banerjee M, Mahiuddin M, Manna PP, Das D. Exploring the scope of photo-induced electron transfer–chelation-enhanced fluorescence–fluorescence resonance energy transfer processes for recognition and discrimination of Zn^{2+}, Cd^{2+}, Hg^{2+}, and Al^{3+} in a Ratiometric manner: application to sea fish analysis. *ACS Omega*. 2018;3(4):4262-4275. (d) Ghorai A, Mondal J, Chandra R, Patra GK. A reversible fluorescent-colorimetric imino-pyridyl bis-Schiff base sensor for expeditious detection of Al^{3+} and HSO_3^- in aqueous media. *Dalton Trans*. 2015;44(29):13261-13271. (e) Ghorai A, Mondal J, Bhattacharya S, Patra GKA. "Chromogenic" and "fluorogenic" bis-Schiff base sensor for rapid detection of hydrazine both in solution and vapour phases. *Anal Methods*. 2015;7(24):10385-10393. (f) Hy L, Py C, Cf W, At W. A turn-on and reversible fluorescence sensor for zinc ion. *Analyst*. 2012;137(19):4415-4417. (g) Banerjee A, Sahana A, Lohar S, et al. A rhodamine derivative as a "lock" and SCN^- as a "key": visible light excitable SCN^- sensing in living cells. *Chem Commun*. 2013;49(25):2527-2529. (h) Long GL, Winefordner JD. Limit of detection. A closer look at the IUPAC definition. *Anal. Chem*. 1983;55(7):712A-724A.
3. Agency for Toxic Substances and Disease Registry (ATSDR). *Toxicological profile for naphthalene*. Atlanta, GA: U. S. Department of Health and Human Services; 1996.
4. Aldini G, Dalle-Donne I, Colombo R, Facino RM, Milzani A, Carini M. Lipoxidation-derived reactive carbonyl species as potential drug targets in preventing protein Carbonylation and related cellular dysfunction. *Chem Med Chem*. 2006;1(13):1045-1058.
5. Andreoli R, Manini P, Bergamaschi E, Mutti A, Franchini I, Niessen WMA. Determination of naphthalene metabolites in human urine by liquid chromatography–mass spectrometry with electrospray ionization. *J Chromatogr*. 1999;847(1–2):9-17.
6. Figueira-Duarte TM, Müllen K. Pyrene-based materials for organic electronics. *Chem Rev*. 2011;111(11):7260-7314.
7. McCallister MM, Maguire M, Ramesh A, et al. Prenatal exposure to benzo(a) pyrene impairs later-life cortical neuronal function. *Neuro Toxicol*. 2008;29(5):846-854.
8. Goldman R, Enewold L, Pellizzari E, et al. Smoking increases carcinogenic polycyclic aromatic hydrocarbons in human lung tissue. *Cancer Res*. 2001;61(17):6367-6371.
9. (a) Zhang J, Chang L, Jin H, et al. Benzopyrene promotes lung cancer A549 cell migration and invasion through up-regulating cytokine IL8 and chemokines CCL2 and CCL3 expression. *Exp Biol Med*. 2016;241(14):1516-1523. (b) Zhang Z, Zhang Z, Lu H, et al. Microglial polarization and inflammatory mediators after intracerebral hemorrhage. *Mol Neurobiol*. 2017;54(3):1874-1886.
10. (a) Penning T, Burczynski M, Hung CF, McCoull D, Palackal N, Tsuruda S. Dihydrodiol Dehydrogenases and Polycyclic aromatic hydrocarbon activation: generation of reactive and redox active o-Quinones. *Chem Res Toxicol*. 1999;12(1):1-18. (b) Platt KL, Aderhold S, Kulpe K, Fickler M. Unexpected DNA damage caused by polycyclic aromatic hydrocarbons under standard laboratory conditions. *Mutat Res*. 2008;650(2):96-103.
11. Senkan S, Castaldi M. Combustion. In: *Ullmann's Encyclopedia of Industrial Chemistry*. Weinheim: Wiley-VCH; 2003.
12. Marti AA, Li X, Jockusch S, et al. Pyrene binary probes for unambiguous detection of mRNA using time-resolved fluorescence spectroscopy. *Nucleic Acids Res*. 2006;34(10):3161-3168.
13. Conlon PC, Yang J, Wu Y, et al. Pyrene excimer signaling molecular beacons for probing nucleic acids. *J Am Chem Soc*. 2008;130(1):336-342.
14. (a) Detriche S, Devillers S, Seffer JF, Nagy JB, Mekhalif Z, Delhalle J. The use of water-soluble pyrene derivatives to probe the surface of carbon nanotubes. *Carbon*. 2011;49(9):2935-2943. (b) Yang K, Wang X, Zhu L, Xing B. Competitive sorption of pyrene, Phenanthrene, and naphthalene on multiwalled carbon nanotubes. *Environ Sci Technol*. 2006;40(18):5804-5810. (c) Teoh HW, Mammucari R, Vieira de Melo Silvio AB, Foster NR. Solubility and solubility modeling of polycyclic aromatic hydrocarbons in subcritical water. *Ind Eng Chem Res*. 2013;52(16):5806-5814. (d) Teoh HW, Vieira de Melo Silvio AB, Mammucari R, Foster NR. Solubility and solubility modeling of polycyclic aromatic hydrocarbons in subcritical ethanol and water mixtures. *Ind. Eng. Chem. Res*. 2014;53(24):10238-10248. (e) Polynuclear aromatic hydrocarbons in Drinking-water, Background document for development of WHO Guidelines for Drinking-water Quality. In: *Addendum to Vol. 2. Health criteria and other supporting information. World Health Organization*. 2nd ed. Geneva; 1998.
15. IARC Monographs, Supplement/World Health Organization. *International Agency for Research on Cancer*. 1987;7:1-440.
16. (a) Sinha R, Kulldorff M, Gunter MJ, Strickland P, Rothman N. Dietary benzo [a] pyrene intake and risk of colorectal adenoma. *Adenoma Cancer Epidemiol Biomarkers Prev*. 2005;14(8):2030-2034. (b) Denissenko MF, Pao A, Tang M, Pfeifer GP. Preferential formation of benzo [a] pyrene adducts at lung Cancer mutational hotspots in P53. *Science*. 1996;18(5286):430-432.
17. Gündel J, Angerer J. High-performance liquid chromatographic method with fluorescence detection for the determination of 3-hydroxybenzo [a] pyrene and 3-hydroxybenz [a] anthracene in the urine of polycyclic aromatic hydrocarbon-exposed workers. *J Chromatogr B Biomed Sci Appl*. 2000;738(1):47-55.
18. Perry M, Carra C, Chre'tien MN, Scaiano JC. Effect of Hexafluorobenzene on the Photophysics of pyrene. *J Phys Chem a*. 2007;111(23):4884-4889.
19. Klajn R, Stoddart JF, Grzybowski B. Nanoparticles functionalised with reversible molecular and supramolecular switches. *Chem Soc Rev*. 2010;39(6):2203-2237.
20. Kathiravan A, Sundaravel K, Jaccob M, et al. Pyrene Schiff Base: photophysics, aggregation induced emission, And Antimicrobial Properties. *J Phys Chem B*. 2014;118(47):13573-13581.

21. Samanta S, Goswami S, Hoque MN, Ramesh A, Das G. An aggregation-induced emission (AIE) active probe renders Al (III) sensing and tracking of subsequent interaction with DNA. *Chem Commun*. 2014;50(80):11833-11836.
22. Ghosh M, Mandal S, Ta S, Das D. Detection and discrimination of Al^{3+} and Hg^{2+} using a single probe: Nano-level determination, human breast cancer cell (MCF7) imaging, binary logic gate development and sea fish sample analysis. *Sens Actuators B: Chem*. 2017;249:339-347.
23. Ghosh A, Sengupta A, Chattopadhyay A, Das D. Lysine triggered ratiometric conversion of dynamic to static excimer of a pyrene derivative: aggregation-induced emission, nanomolar detection and human breast cancer cell (MCF7) imaging. *Chem Commun*. 2015;51(57):11455-11458.
24. Zhang DD, Feng JJ, Liu YF, et al. Enhanced hole injection in organic light-emitting devices by using Fe_3O_4 as an anodic buffer layer. *Appl Phys Lett*. 2009;94(22):223306.
25. Xia H, Li M, Lu D, et al. Host selection and configuration design of electrophosphorescent devices. *Adv Funct Mater*. 2007;17(11):1757-1764.
26. (a) Bruchez JM, Moronne M, Gin P, Weiss S, Alivisatos AP. Semiconductor nanocrystals as fluorescent biological labels. *Science*. 1998;281(5385):2013-2016. (b) Chan WCW, Nie S. Quantum dot bioconjugates for ultrasensitive nonisotopic detection. *Science*. 1998;281(5385):2016-2018. (c) Maity A, Das S, Mandal S, Gupta P, Purkayasth P. Interaction of semicarbazide and thiosemicarbazide pyrene derivatives with anionic and cationic micelles: changed character of pyrene due to alteration in charge density induced by the side chains. *RSC Adv*. 2013;3(30):12384-12389. (d) Feng X, Qi C, Feng HT, et al. Dual fluorescence of tetraphenylethylene-substituted pyrenes with aggregation-induced emission characteristics for white-light emission. *Chem Sci*. 2018;9(25):5679-5687. (e) Siu H, Duhamel J. Molar absorption coefficient of pyrene aggregates in water. *J Phys Chem B*. 2008;112(48):15301-15312. (f) Zhang DD, Feng J, Wang H, et al. Improved hole injection and transport of organic light-emitting devices with an efficient p-doped hole-injection layer. *Appl Phys Lett*. 2009;95(26):263303-263307.
27. (a) Ghosh M, Ghosh A, Ta S, Matalobos JS, Das D. ESIPT-based Nanomolar Zn^{2+} sensor for human breast Cancer cell (MCF7) imaging. *Chemistry Select*. 2017;2(24):7426-7431. (b) Adhikari S, Ghosh A, Ghosh M, Guria S, Das D. Ratiometric sensing of Fe^{3+} through PET-CHEF-FRET processes: live cell imaging, speciation and DFT studies. *Sens and Actuators B: Chem*. 2017;251:942-950.
28. (a)Ghosh A, Ta S, Ghosh M, et al. Dual mode ratiometric recognition of zinc acetate: nanomolar detection with in vitro tracking of endophytic bacteria in rice root tissue. *Dalton Trans*. 2016;45(2):599-606. (b) Ghosh M, Ta S, Matalobos Jesús S, Das D. Azine based smart probe for optical recognition and enrichment of Mo (VI). *Dalton Trans*. 2018;47(32):11084-11090. (c) Ghosh M, Ta S, Banerjee M, et al. Recognition of ceric ion in aqueous medium at pico-molar level: colorimetric, fluorimetric and single crystal X-ray structural evidences. *J Photochem Photobiol a*. 2018;367:32-38.
29. Ringer AL, MacKerell AD. Calculation of the vibrational stark effect using a first-principles quantum mechanical/molecular mechanical approach. *J Phys Chem Lett*. 2011;2(6):553-556.
30. Hong Y, Lam JWY, Tang BZ. Aggregation-induced emission: phenomenon, Mechanism and Applications. *Chem Commun*. 2009;29(29):4332-4353.
31. Zhao Z, Chen S, Lam JWY, et al. Pyrene-substituted ethenes: aggregation-enhanced excimer emission and highly efficient electroluminescence. *J Mater Chem*. 2011;21(20):7210-7216.

SUPPORTING INFORMATION

Additional supporting information may be found online in the Supporting Information section at the end of the article.

How to cite this article: Ghosh M, Ta S, Lohar S, et al. Exploring aggregation-induced emission through tuning of ligand structure for picomolar detection of pyrene. *J Mol Recognit*. 2018;e2771. https://doi.org/10.1002/jmr.2771